Open Access

32-Gb/s OOK and 64-Gb/s PAM-4 Modulation Using a Single-Drive Silicon Mach–Zehnder Modulator with 2 V Drive Voltage

Volume 11, Number 6, December 2019

Gangqiang Zhou
Linjie Zhou
Yuyao Guo
Shuhuang Chen
Liangjun Lu
Lei Liu
Jianping Chen

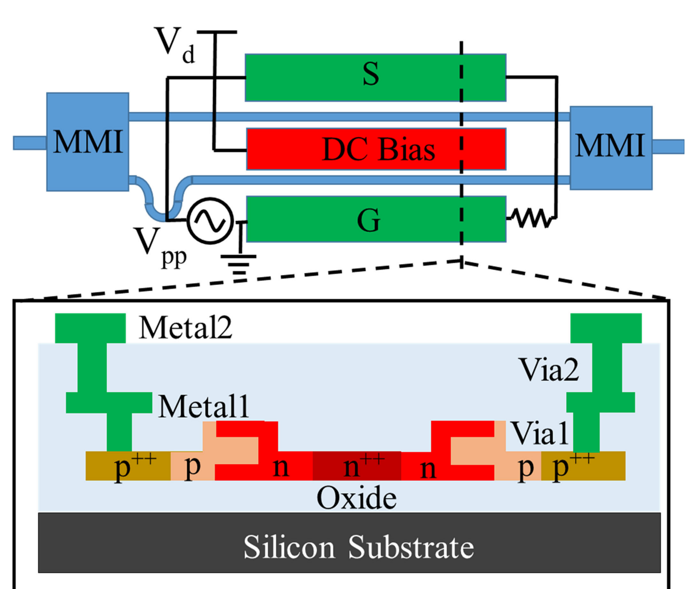

DOI: 10.1109/JPHOT.2019.2954597

32-Gb/s OOK and 64-Gb/s PAM-4 Modulation Using a Single-Drive Silicon Mach–Zehnder Modulator with 2 V Drive Voltage

Gangqiang Zhou,[1] Linjie Zhou,[1] Yuyao Guo,[1] Shuhuang Chen,[1] Liangjun Lu,[1] Lei Liu,[2] and Jianping Chen[1]

[1]Shanghai Institute for Advanced Communication and Data Science, Shanghai Key Lab of Navigation and Location Services, State Key Laboratory of Advanced Optical Communication Systems and Networks Department of Electronic Engineering, Shanghai Jiao Tong University, Shanghai 200240, China
[2]Transmission Technology Research Department, Huawei Technologies Co. Ltd., Shenzhen 518129, China

DOI:10.1109/JPHOT.2019.2954597
This work is licensed under a Creative Commons Attribution 4.0 License. For more information, see https://creativecommons.org/licenses/by/4.0/

Manuscript received July 18, 2019; revised October 19, 2019; accepted November 17, 2019. Date of publication November 20, 2019; date of current version December 13, 2019. This work was supported in part by the National Natural Science Foundation of China under Grants 61705129 and 61535006, in part by the National Key R&D Program of China under Grant 2018YFB2201702, and in part by Shanghai Municipal Science and Technology Major Project under Grant 2017SHZDZX03.
Corresponding author: Linjie Zhou (e-mail: ljzhou@sjtu.edu.cn).

Abstract: We demonstrate a high-efficiency silicon Mach-Zehnder modulator with U-shaped PN junctions. The depletion region of the U-shaped PN junction has a large overlap with the waveguide optical mode, leading to a low drive voltage. The calculated modulation efficiency is 0.33 V·cm at 0 V bias and 0.55 V·cm at −2 V bias. On-off keying (OOK) modulation and four-level pulse amplitude modulation (PAM-4) are achieved at 32 Gb/s and 64 Gb/s data rates under 2 V drive voltage, respectively. The bit error rate for the PAM-4 modulation is below the hard-decision forward error correction threshold of 3.8×10^{-3}.

Index Terms: Silicon modulator, silicon photonics, Mach-Zehnder modulator, PAM-4 modulation, OOK modulation, U-shaped PN junction, high modulation efficiency.

1. Introduction

In recent years, silicon photonics has developed rapidly, due to its compatibility with low-cost complementary-metal-oxide-semiconductor (CMOS) manufacturing processes. It has great potential for monolithic photonics-electronic integration. Among various silicon photonics devices, high-speed silicon electro-optic (EO) modulators have been extensively investigated, since they are the core devices in optical transmitters [1]. Refractive index modulations based on carrier depletion, carrier injection, and carrier accumulation are three key methods to realize EO modulators on the silicon photonics platform. Carrier-injection-based modulators enabled by PIN junctions offer high modulation efficiency. However, the speed of this kind of modulators is usually limited to a few Gbit/s without using pre-emphasis techniques [2]–[4]. Modulators based on the carrier-accumulation effect possess both high modulation efficiency and high bandwidth [5]–[7]. A silicon Mach-Zehnder modulator (MZM) integrated with vertical metal-oxide-semiconductor (MOS) capacitors has been demonstrated to achieve $V_\pi \cdot L$ ($V_\pi \cdot L = \pi \cdot V_{bias} \cdot L/\Delta\varphi$, where $\Delta\varphi$ is the phase shift at V_{bias} and

L is the phase shifter length) of 0.2 V·cm and OOK modulation speed up to 40 Gb/s under 1-V drive voltage [6]. A silicon MZM with lateral MOS-capacitors has also been reported to have $V_\pi \cdot L$ of 1.53 V·cm and OOK modulation speed up to 25 Gb/s with 6-V drive voltage [7]. However, the fabrication process of this kind of modulators is very complicated, increasing the device cost.

The carrier-depletion-based modulators have a large modulation bandwidth with a relatively simple fabrication process compared to the MOS structures [8]–[12]. By optimizing the PN junction profile in the waveguide cross-section, the modulation efficiency can be improved. Various shapes of PN junctions have been developed such as interdigitated PN junctions [13]–[16], vertical PN junctions [17], [18], L-shaped PN junctions [12], [19], [20], and U-shaped PN junctions [21], [22]. The MZM [15] and micro-ring modulator (MRM) [16] with interdigitated PN junctions can provide 10 Gb/s and 25 Gb/s OOK modulation with 3 V and 2 V drive voltages, respectively. However, the interdigitated PN junctions require stringent control of ion implantation windows. The modulator with vertical PN junctions has $V_\pi \cdot L$ of 0.75 V·cm and modulate only at 16 Gb/s with 2 V drive voltage [18]. A high bit rate up to 64 Gb/s has been demonstrated using a MRM, in which the L-shaped PN junction improves the $V_\pi \cdot L$ to 0.52 V·cm at a bias voltage of -2 V [12]. However, the fabrication tolerance of MRMs is low. Besides, a feedback control circuit is required to stabilize the operation point of MRMs. The MZM with L-shaped PN junctions has $V_\pi \cdot L$ of 0.81 V·cm at -2.5 V bias, allowing for 10 Gb/s OOK modulation [20]. Compared with L-shaped PN junction, U-shaped PN junction can give a higher modulation efficiency .The MZM with U-shaped PN junctions has a $V_\pi \cdot L$ of 0.46 V·cm at -0.5 V and 0.94 V·cm at -2 V, achieving only 24 Gb/s OOK modulation in the O-band [22]. Michelson interferometer (MI)-based modulators could also have an improved modulation efficiency as light passes through the modulation arm twice [23], [24]. OOK modulation up to 34 Gb/s has been demonstrated with a 3.4 V drive voltage [24].

Although the optical signal-to-noise ratio required for OOK modulation is lower than that of PAM-4 modulation [25], achieving ultra-high bit rate OOK modulation has become difficult due to the large bandwidth requirements. At the same baud rate, the bit rate of PAM-4 modulation is twice that of OOK modulation, thus reducing the bandwidth requirements. Direct detection can be also used for PAM-4 modulation as in OOK modulation, simplifying the detection scheme. In addition, PAM-4 modulation has lower power consumption per bit, assuming no increase in drive voltage requirements [10]. Various types of modulators can be used to generate PAM-4 signals, including dual-drive Mach-Zehnder modulator (DDMZM) [8], [26], [27], single-drive Mach-Zehnder modulator (SDMZM) [9], [11], dual-drive Michelson interferometric modulator (DDMIM) [28], dual-parallel Mach-Zehnder modulator (DPMZM) [29], segmented-electrode Mach-Zehnder modulator (SEMZM) [30], [31], MRM [12], [19], cascaded MRM (CMRM) [32], micro-ring resonator assisted Mach-Zehnder modulator (RAMZM) [33], [34], and so on. The drive voltage is usually large [25]–[34], due to the relatively low $V_\pi \cdot L$ of the regular PN junction. Currently, 8×50 G PAM-4 over 2 km of standard single-mode fiber (SSMF) transmission (400GBASE-FR8) has been accepted for the next 400G Ethernet [35]. In this case, a modulator supporting 50+ Gb/s PAM-4 signals is required. Therefore, it is necessary to realize 50+ Gb/s PAM-4 MZMs with a low drive voltage.

In this work, we present a silicon MZM with U-shaped PN junctions to achieve both low $V_\pi \cdot L$ and high modulation speed in the C-band. The $V_\pi \cdot L$ is 0.34–0.55 V·cm at the bias voltages of 0 V to -2 V. OOK and PAM-4 modulations with data rates of 32 Gb/s and 64 Gb/s are successfully demonstrated with 2-V drive voltage, respectively.

2. Device Structure and Simulation

2.1 Mach–Zehnder Modulator Structure

Fig. 1 shows the schematic structure of the MZM. Two 3-dB multimode interferometers (MMIs) are used as the input splitter and the output combiner in this modulator. To achieve a high modulation bandwidth, we adopt the single-drive push-pull traveling-wave electrode (TWE) design. The active arm integrated with a U-shaped PN junction has a length of 3 mm and the arm length difference is 90 μm. Therefore, by changing the optical wavelength, we could change the operation point of the

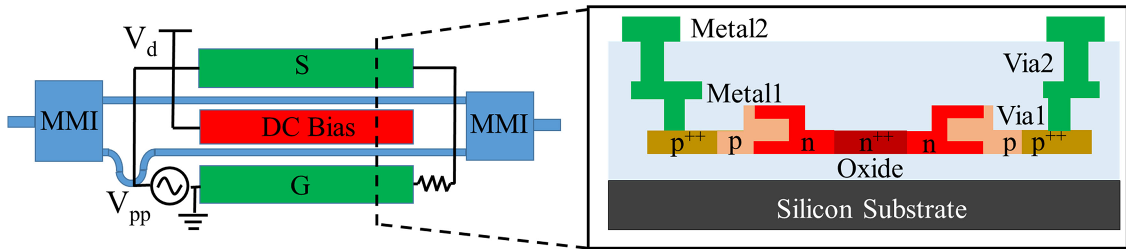

Fig. 1. Schematic structure of the modulator. The inset shows the cross-section of the modulation arm.

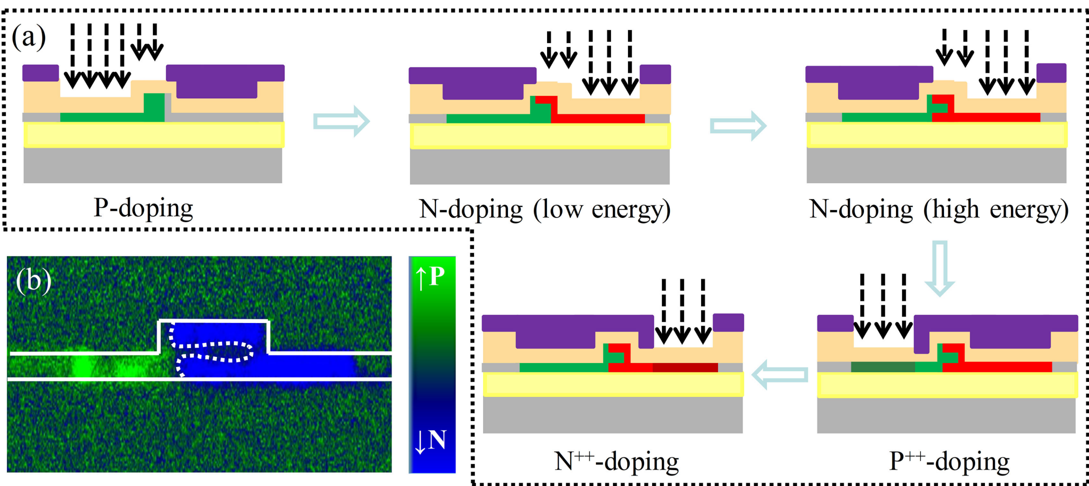

Fig. 2. (a) Doping process to form U-shaped PN junction. (b) SCM image of the MZM modulation arm.

MZM. The inset shows the cross-sectional structure of the modulation arms. The waveguide width is 500 nm and the height is 220 nm. The thickness of the slab is 90 nm. The p^{++}-doping regions are connected to the ground (G) and signal (S) lines of the TWE, which is composed of two layers of aluminum metals. The distance between the heavy-doping regions and the edge of the optical waveguide is 500 nm. We used COMSOL Multiphysics software to optimize the design of the TWE [36]. The width and height of the metal2 layer are 30 μm and 2 μm, respectively. The gap distance between the two metal2 lines is 45 μm. The metal1 is used to facilitate electrical connections. A DC bias line is connected to the n^{++}-doping region in the middle of the two arms. A bias voltage is applied through the DC bias line to keep the PN junctions in the reverse-bias condition.

2.2 Simulation of U-shaped PN Junction

To form the U-shaped PN junction, three light-doping and two heavy-doping steps are used, as shown in Fig. 2(a). The silicon is first covered with a 10-nm-thick SiO_2 layer to reduce the channeling effect during ion implantation. The first step is to form uniform p-type doping in the waveguide using Boron implantation. Next, the waveguide is n-type doped at the top using phosphorous implantation of low energy. Then, n-type doping is performed at the bottom of the waveguide with high implantation energy. Finally, heavy doping is performed to form the n^{++} and p^{++}-doping regions. It should be noted that the same mask is used for the waveguide top and bottom n-type light doping. We took the scanning capacitance microscopy (SCM) image of the doping profile in the modulation waveguide, as shown in Fig. 2(b). The U-shaped PN junction is clearly discerned inside the waveguide. It has a strong overlap with the waveguide optical mode, resulting in low a $V_\pi \cdot L$.

TABLE 1
Ion Implantation Conditions for the U-Shaped PN Junction

Step	Dopants	Dose (ions/cm^2)	Energy (keV)	Window (μm)
1	Boron	4.5e13	20	[1,6.43]
2	Phosphorus	3e13	22	[6.07,11.5]
3	Phosphorus	2.5e13	100	[6.07,11.5]
4	Boron	3e15	15	[1,5.5]
5	Phosphorous	1e15	25	[7,11.5]

The waveguide location is [6, 6.5] (μm) in the simulation.

We employed the semiconductor TCAD tool to simulate the fabrication process of the U-shaped PN junction. Then, we exported the electron and hole concentrations to COMSOL to simulate V_π and doping-induced loss. According to the simulated V_π and loss, we optimized the ion implantation conditions for the U-shaped PN junction, as shown in Table 1. The n-type and p-type doping concentrations of the PN junctions are $\sim$2 $\times$ 10^{18} cm^{-3} and $\sim$1 $\times$ 10^{18} cm^{-3}, respectively. In order to form a good ohmic contact, the n^{++}- and p^{++}-doping concentrations are set as $\sim$1 $\times$ 10^{20} cm^{-3}. Fig. 3 shows the influence of implantation dose and energy on V_π and loss. The insets show the simulated free-carrier distributions in the PN junction under -2 V bias. The shape and position of the PN junction vary with the ion implantation dose and energy, and as a result, the loss and V_π also change accordingly. To get low loss and low V_π, it is necessary to stringently control the dose and energy, especially for the second implantation step.

3. Experimental Results

3.1 Direct-Current (DC) Characterization

Fig. 4(a) shows the transmission spectra of the MZM at various reverse bias voltages on one arm. It was normalized to a straight waveguide. The light was set to TE polarization before coupling to the chip using a lensed fiber. The on-chip insertion loss at 0-V bias is approximately 9.8 dB, consisting of 0.2 dB loss from the MMIs, 2.1 dB loss from the passive silicon waveguide, and 7.5 dB loss from the 3-mm-long phase shifter. The static extinction ratio is about 25 dB at 0-V bias, indicating a relatively balanced power of the two arms. Fig. 4(b) illustrates the extracted phase shift as a function of bias voltage. The π phase shift is achieved at a reverse bias voltage of 1.7 V, corresponding to a $V_\pi \cdot L$ of 0.51 V·cm. The small-signal $V_\pi \cdot L$ is 0.34 V·cm and 0.55 V·cm at 0 and -2 V biases, respectively.

3.2 EE and EO Characterization

We measured the electro-electro (EE) S-parameters of the TWE at various DC bias voltages using a 67-GHz vector network analyzer (VNA, Keysight, N5247A). A pair of 40-GHz GS probes were used to connect the VNA and the modulator. The probes were calibrated using a standard calibration substrate (GGB, CS-8) before measurement. Figs. 5(a) and 5(b) show the measured EE-S_{21} and EE-S_{11} curves of the TWE. The EE-S_{21} curve was normalized to 100 MHz frequency point. The 6.4 dB bandwidth is increased from 18.6 GHz to 27.7 GHz when the bias voltage varies from -2 V to -4 V. The RF reflection is below -10 dB from 100 MHz to 40 GHz, indicating reasonably good impedance match between the modulator TWE and the RF cable. Then, we used the VNA and a 50 GHz photodiode (PD, U^2t, XPDV2120R) to measure the electro-optic (EO) S-parameters of the modulator under various bias voltages, as shown in Fig. 5(c). The 3-dB bandwidth is 14.7 GHz at -2 V bias. Because of the U-shaped PN junction, the junction capacitance is large, leading to

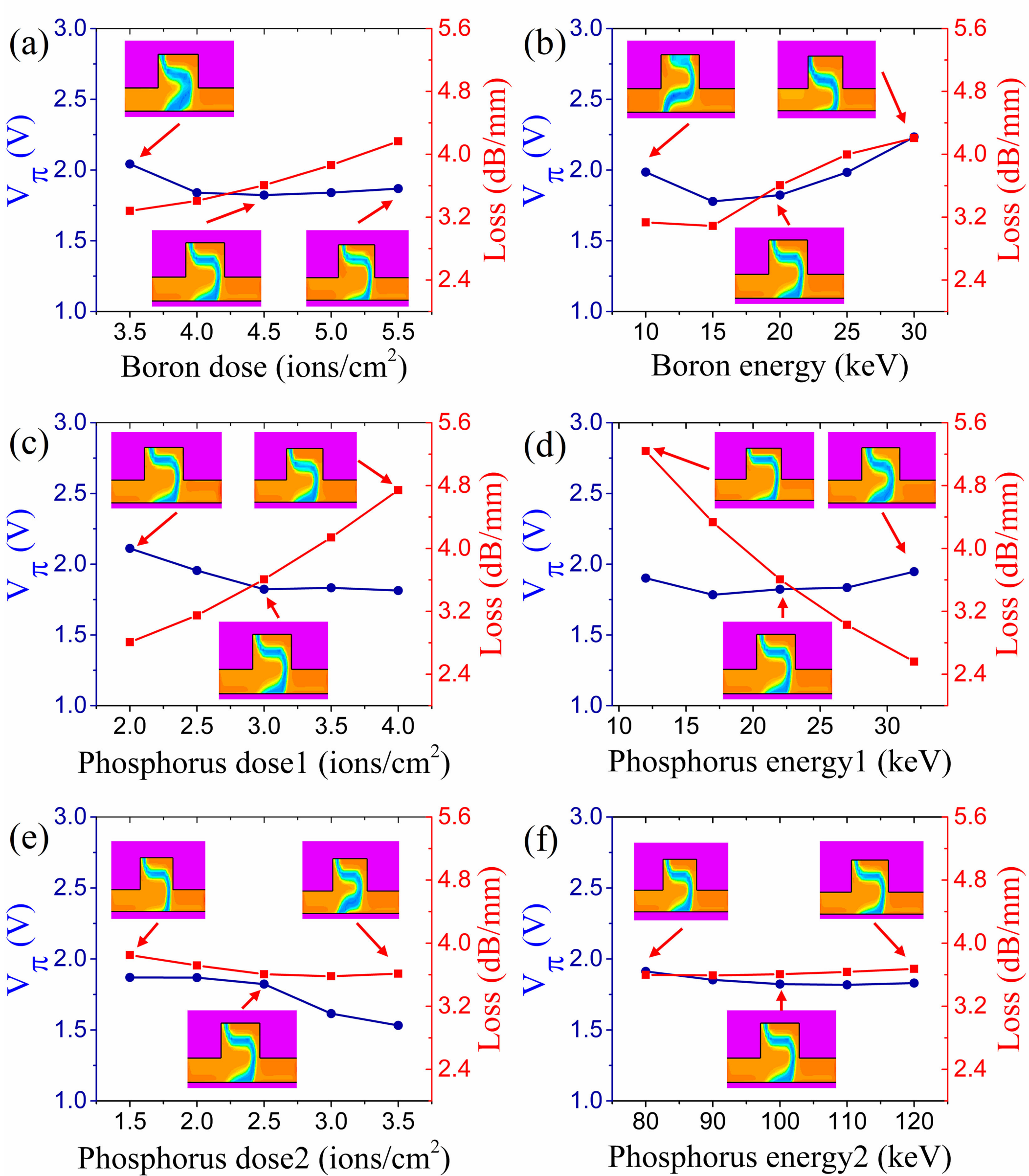

Fig. 3. Simulated V_π and Loss as a function of the dose and energy in (a, b) the first implantation step, (c, d) the second implantation step, and (e, f) the third implantation step. The insets show the free-carrier distributions in the PN junction under −2 V bias.

a higher modulation efficiency but at the expense of a reduced EO bandwidth of the modulator [21], [37]. In general, for Mach-Zehnder modulators with carrier-depletion-based PN junctions, in order to get a high modulation efficiency, we should enlarge the overlap between the optical modal field and the carrier depletion region. On the other hand, a large depletion region also results in an increased junction capacitance, lowering the EO bandwidth of the modulator. The modulation efficiency is independent of the modulation arm length. For a fixed arm length, the drive voltage is reduced for a modulator with a higher modulation efficiency. For a certain PN junction, the drive voltage of the modulator decreases with the increasing arm length. However, the EO bandwidth of the modulator also becomes narrower with a longer arm length.

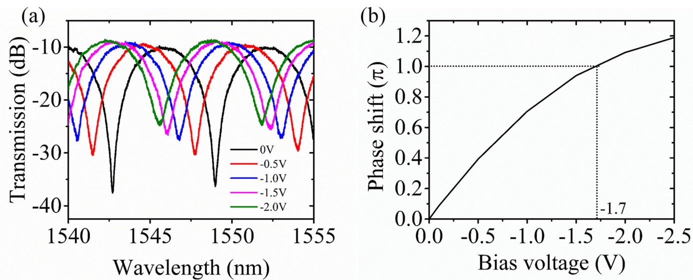

Fig. 4. (a) Measured transmission spectra of the MZM under various reverse bias voltages. (b) Extracted phase shift as a function of bias voltage.

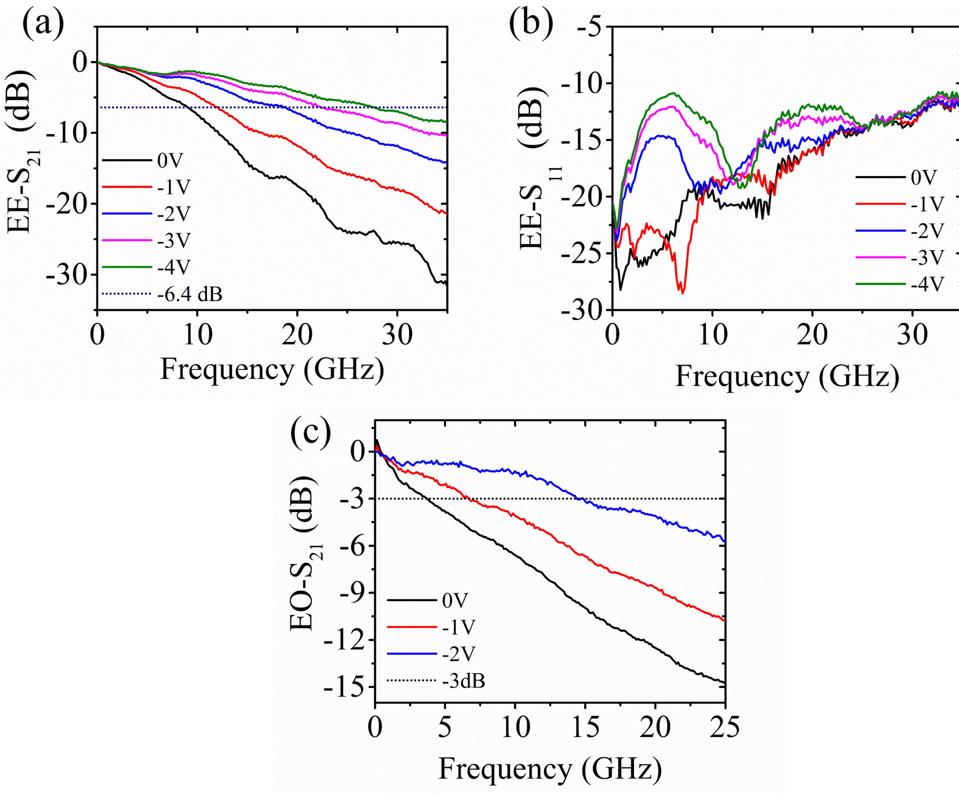

Fig. 5. (a) EE-S_{21}, (b) EE-S_{11}, and (c) EO-S_{21} responses of the MZM at various DC biases.

3.3 OOK and PAM4 Modulations

Fig. 6 shows the experimental setup for high-speed OOK and PAM-4 modulations using the MZM. The device was fabricated on a high-resistivity SOI wafer with a top silicon layer thickness of 220 nm and a buried-oxide (BOX) layer thickness of 2 μm using CMOS-compatible processes. The wavelength of the input light from a tunable continuous-wave laser was set around 1550.31 nm at the quadrature point of the MZM. The modulated optical signal was amplified by an erbium-doped optical amplifier (EDFA) and followed by an optical filter. It was finally detected by a 50-GHz PD and received by a digital communication analyzer (DCA, Agilent DCA-X 86100D). For OOK modulation, the modulator was driven by a pseudo-random binary sequence (PRBS-31) signal generated from a pulse pattern generator (PPG, Keysight, N4960A, N4951B). The peak-to-peak voltage (V_{pp}) of the PRBS-31 signal was set to 2 V. The PRBS signal was applied to the modulator through the

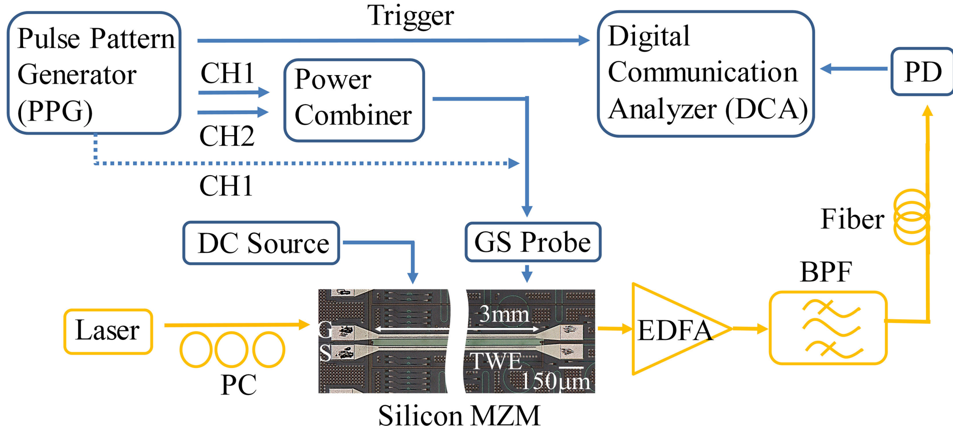

Fig. 6. Experimental setup for OOK and PAM4 modulations.

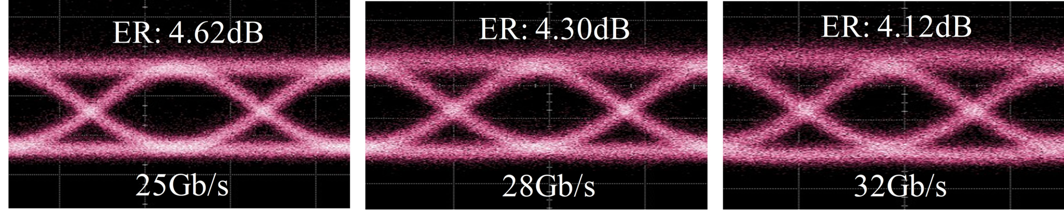

Fig. 7. Eye diagrams of the modulated 25 Gb/s, 28 Gb/s, and 32 Gb/s OOK signals after B2B transmission.

40-GHz GS probes. The other end of the MZM was terminated with an external 50 Ω resistor. For PAM-4 modulation, the modulator was driven by a PAM-4 signal generated by combing two independent PRBS-31 signals through an RF power combiner. The peak-to-peak voltages of the two PRBS-31 signals were 1 V and 2 V. The average optical power received by the PD is 1 dBm in the OOK modulations. In PAM-4 modulation, in order to get a lower bit error rate (BER), the optical power received by the PD is increased to 5 dBm after adjusting the EDFA gain. The DC bias voltage is fixed at 2 V. Fig. 7 shows the OOK modulation eye diagrams after B2B transmission. The modulation extinction ratio (ER) and the signal-to-noise ratio (SNR) are 4.12 dB and 4.66 dB at the data rate of 32 Gb/s.

Fig. 8 shows the PAM-4 eye-diagrams at 25 GBaud/s, 28 GBaud/s, and 32 GBaud/s. The DCA offers the average voltage and variance of each individual level of the PAM-4 signal according to the histograms. The four average voltages obtained at 32 GBaud/s after 2-km single-mode-fiber (SMF) transmission are 79.5 mV, 59.8 mV, 45.2 mV, 30.6 mV. The BER was calculated by assuming the noise has a Gaussian distribution. This method is accurate enough to match the BER from error counting [38]. The BERs at 25 GBaud/s after B2B transmission and 2-km fiber transmission are 5.45×10^{-4} and 1×10^{-3} respectively. The BERs at 32 GBaud/s after B2B transmission and 2-km fiber transmission increase to 3.0×10^{-3} and 3.4×10^{-3}, respectively, still below the hard-decision forward error correction (HD FEC) threshold of 3.8×10^{-3}. These results show that this modulator could support 50+ Gb/s PAM-4 signal.

4. Discussion

Tables 2 and 3 compare our work with some of the state-of-the-art silicon OOK modulators with carrier-depletion PN junctions and DSP-free silicon PAM-4 modulators. It can be seen that the

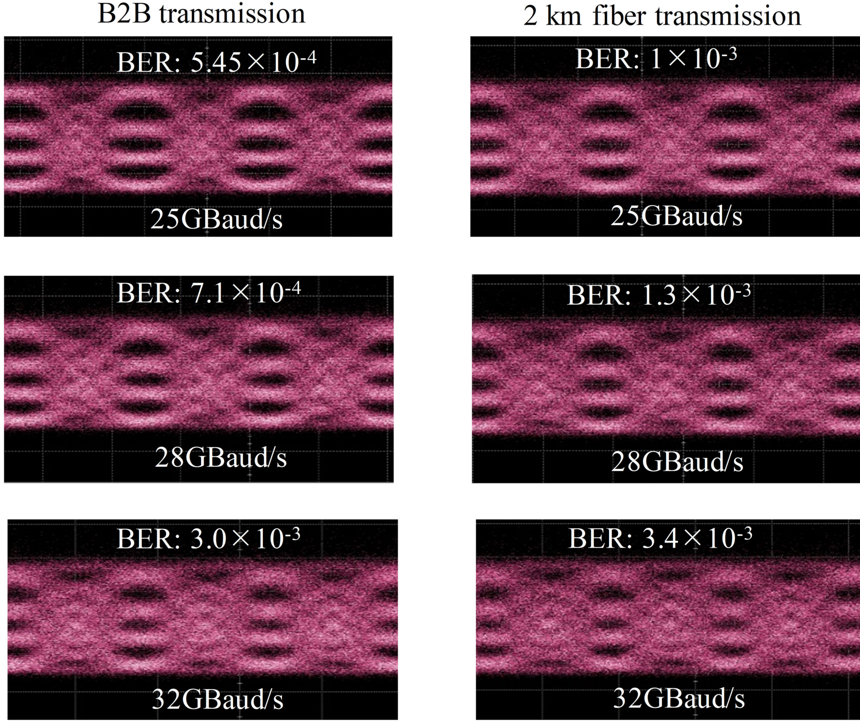

Fig. 8. Eye diagrams of the modulated 25 GBaud/s, 28 GBaud/s, and 32 GBaud/s PAM-4 signals. The left column shows the results after B2B transmission and the right column shows the results after 2 km fiber transmission.

TABLE 2
Performance Comparison of Silicon OOK Modulators With Carrier-Depletion PN Junctions

Reference	Structure	Operation Band	Bandwidth (GHz)	$V_{\pi}\cdot L$ (V·cm)	Speed (Gb/s)	ER (dB)	V_{pp} (V)
[16]	MRM	C-band	11.8 (-1V)	0.68-1.64	25	4.5	2
[12]	MRM	O-band	50 (-2V)	0.4-0.52	64	4.8	2.5
[24]	MIM	C-band	11.3 (-2V)	0.72-1	34	4.0	3.4
[15]	MZM	C-band	2.6 (0V)	0.62-0.96	10	7.5	3
[18]	MZM	C-band	NA	0.75	16	NA	2
[20]	MZM	C-band	12 (-3V)	0.81	10	>10	3.3
[22]	MZM	O-band	13 (-2V)	0.46-0.94	24	2.2	2.88
[9]	MZM	C-band	58 (-4V)	1.4	90	3.3	5
This work	**MZI**	**C-band**	**14.7 (-2V)**	**0.33-0.51**	**32**	**4.1**	**2**

MRMs have the potential for high-speed modulation with low drive voltage. The MZMs have better process tolerance and temperature stability compared to MRMs. Our modulator possesses both high modulation efficiency and high bandwidth. With 2-V drive voltage, we can successfully realize OOK and PAM-4 modulations with 32 Gb/s and 64 Gb/s data rates, respectively. To the best of our knowledge, among the silicon DSP-free PAM-4 modulators that could support 50+ Gb/s PAM-4 signals, the drive voltage of our modulator is the lowest. Recently, thin-film integrated lithium niobate electro-optic modulators have been developed, exhibiting a CMOS-compatible drive voltage, a large bandwidth, and a low insertion loss [39], [40]. However, they typically have a modulation arm length

TABLE 3
Performance Comparison of DSP-Free Silicon PAM-4 Modulators

Reference	Structure	Band	V_{pp} (V)	Bit rate (Gb/s)	Transmission (km)	BER
[12]	MRM	O-band	2.4	128	NA	NA
[34]	RAMZM	C-band	3.19,4.26	50	2	3.3×10^{-3}
[31]	SEMZM	C-band	4.8,4.8	100	1	$<3.8\times10^{-3}$
[27]	DDMZM	C-band	5	70	0	6.6×10^{-5} (64Gb/s)
[26]	DDMZM	C-band	1.5,3	64	0	2.2×10^{-6} (50Gb/s)
[11]	SDMZM	C-band	7	80	0	1.23×10^{-2}
[29]	DP-MZM	C-band	2,4	100	2	$<4.4\times10^{-3}$
[28]	DDMIM	C-band	1.41,4.92	56	2	1.4×10^{-3}
This work	**SDMZM**	**C-band**	**2V**	**64**	**2**	$\mathbf{3.4\times10^{-3}}$

In [11], [28], [29], [31], [34] and this work, the BER was estimated by using histograms of the captured eye diagrams.
In [26], [27], the BER was measured by error counting using real-time oscilloscopes.

of up to 10 mm in order to get a low drive voltage of 2 V, because the $V_\pi \cdot L$ is greater than 2 V·cm. The silicon electro-optic modulators possess the key inherent merits of CMOS compatibility and easy integration with silicon photonic devices and microelectronic drive circuits.

5. Conclusions

We have demonstrated a high-efficiency silicon MZM with U-shaped PN junctions. The measured π phase shift voltage is 1.7 V and the $V_\pi \cdot L$ is 0.51 V·cm. 32 Gb/s OOK modulation and 64 Gb/s PAM-4 modulation were realized using this modulator with only 2-V drive voltage. For a common CMOS driver, the voltage swing (V_{pp}) is usually around 1 V [41], [42]. A large V_{pp} of 3.2 V has been realized using a distributed driver architecture with a standard CMOS process [41], indicating that our modulator with a 2-V drive voltage has the potential to be driven by CMOS circuits, suitable for applications in very-short-reach chip-to-chip optical links.

References

[1] G. T. Reed, G. Mashanovich, F. Y. Gardes, and D. J. Thomson, "Silicon optical modulators," *Nature Photon.*, vol. 4, pp. 518–526, 2010.
[2] Q. Xu, B. Schmidt, S. Pradhan, and M. Lipson, "Micrometre-scale silicon electro-optic modulator," *Nature*, vol. 435, no. 7040, pp. 325–327, 2005.
[3] K. Preston, S. Manipatruni, A. Gondarenko, C. B. Poitras, and M. Lipson, "Deposited silicon high-speed integrated electro-optic modulator," *Opt. Express*, vol. 17, no. 7, pp. 5118–5124, 2009.
[4] K. Debnath *et al.*, "Cascaded modulator architecture for WDM applications," *Opt. Express*, vol. 20, no. 25, pp. 27420–27428, 2012.
[5] J.-H. Han *et al.*, "Efficient low-loss InGaAsP/Si hybrid MOS optical modulator," *Nature Photon.*, vol. 11, pp. 486–490, 2017.
[6] M. Webster, C. Appel, P. Gothoskar, S. Sunder, B. Dama, and K. Shastri, "Silicon photonic modulator based on a MOS-capacitor and a CMOS driver," in *Proc. Compound Semicond. Integr. Circuit Symp.*, 2014, pp. 1–4.
[7] K. Debnath *et al.*, "All-silicon carrier accumulation modulator based on a lateral metal-oxide-semiconductor capacitor," *Photon. Res.*, vol. 6, no. 5, pp. 373–379, 2018.
[8] S. Shao, J. Ding, L. Zheng, L. Zhang, X. Fu, and L. Yang, "90 Gb/s PAM4 and OOK optical signal generation by using the dual-arm-drive silicon Mach-Zehnder modulator," in *Proc. Conf. Lasers Electro-Opt.*, 2018, Paper JW2A.2.
[9] M. Li, L. Wang, X. Li, X. Xiao, and S. Yu, "Silicon intensity Mach-Zehnder modulator for single lane 100 Gb/s applications," *Photon. Res.*, vol. 6, no. 2, pp. 109–116, 2018.

[10] D. Patel *et al.*, "Design, analysis, and transmission system performance of a 41 GHz silicon photonic modulator," *Opt. Express*, vol. 23, no. 11, pp. 14263–14287, 2015.
[11] Y. Zhou, L. Zhou, F. Su, X. Li, and J. Chen, "Linearity measurement and pulse amplitude modulation in a silicon single-drive push-pull Mach–Zehnder modulator," *J. Lightw. Technol.*, vol. 34, no. 14, pp. 3323–3329, Jul. 2016.
[12] J. Sun, R. Kumar, M. Sakib, J. B. Driscoll, H. Jayatilleka, and H. Rong, "A 128 Gb/s PAM4 silicon microring modulator with integrated thermo-optic resonance tuning," *J. Lightw. Technol.*, vol. 37, no. 1, pp. 110–115, Jan. 2019.
[13] D. Marris-Morini *et al.*, "Low loss 40 Gbit/s silicon modulator based on interleaved junctions and fabricated on 300 mm SOI wafers," *Opt. Express*, vol. 21, no. 19, pp. 22471–22475, 2013.
[14] H. Xu *et al.*, "High speed silicon Mach-Zehnder modulator based on interleaved PN junctions," *Opt. Express*, vol. 20, no. 14, pp. 15093–15099, 2012.
[15] H. Yu *et al.*, "Performance tradeoff between lateral and interdigitated doping patterns for high speed carrier-depletion based silicon modulators," *Opt. Express*, vol. 20, no. 12, pp. 12926–12938, 2012.
[16] X. Xiao *et al.*, "25 Gbit/s silicon microring modulator based on misalignment-tolerant interleaved PN junctions," *Opt. Express*, vol. 20, no. 3, pp. 2507–2515, 2012.
[17] M. R. Watts, W. A. Zortman, D. C. Trotter, R. W. Young, and A. L. Lentine, "Low-voltage, compact, depletion-mode, silicon Mach–Zehnder modulator," *IEEE J. Sel. Topics Quantum Electron.*, vol. 16, no. 1, pp. 159–164, Jan./Feb. 2010.
[18] T. Latchu *et al.*, "Power-penalty comparison of push-pull and traveling-wave electrode Silicon Mach-Zehnder modulators," in *Proc. Opt. Interconnects Conf.*, 2014, pp. 25–26.
[19] H. Li *et al.*, "A 112 Gb/s PAM4 transmitter with silicon photonics microring modulator and CMOS driver," in *Proc. Opt. Fiber Commun. Conf. Exhib.*, 2019, Paper Th4A.4.
[20] K. Goi *et al.*, "Low-voltage silicon Mach-Zehnder modulator operating at high temperatures without thermo-electric cooling," in *Proc. Opt. Fiber Commun. Conf. Exhib.*, 2016, Paper W2A.23.
[21] T. Cao, Y. Fei, L. Zhang, Y. Cao, and S. Chen, "Design of a silicon Mach-Zehnder modulator with a U-type PN junction," *Appl. Opt.*, vol. 52, no. 24, pp. 5941–5948, 2013.
[22] Z. Yong *et al.*, "U-shaped PN junctions for efficient silicon Mach-Zehnder and microring modulators in the O-band," *Opt. Express*, vol. 25, no. 7, pp. 8425–8439, 2017.
[23] X. Li *et al.*, "Highly efficient silicon michelson interferometer modulators," *IEEE Photon. Technol. Lett.*, vol. 25, no. 5, pp. 407–409, Mar. 2013.
[24] D. Patel *et al.*, "High-speed compact silicon photonic Michelson interferometric modulator," *Opt. Express*, vol. 22, no. 22, pp. 26788–26802, 2014.
[25] C. Cole, I. Lyubomirsky, A. Ghiasi, and V. Telang, "Higher-order modulation for client optics," *IEEE Commun. Mag.*, vol. 51, no. 3, pp. 50–57, Mar. 2013.
[26] L. Zheng, J. Ding, S. Shao, L. Zhang, and L. Yang, "Silicon PAM-4 optical modulator driven by two binary electrical signals with different peak-to-peak voltages," *Opt. Lett.*, vol. 42, no. 11, pp. 2213–2216, 2017.
[27] S. Shao *et al.*, "Optical PAM-4 signal generation using a silicon Mach-Zehnder optical modulator," *Opt. Express*, vol. 25, no. 19, pp. 23003–23013, 2017.
[28] R. Li *et al.*, "Silicon photonic dual-drive MIM based 56 Gb/s DAC-less and DSP-free PAM-4 transmission," *Opt. Express*, vol. 26, no. 5, pp. 5395–5407, 2018.
[29] A. Samani, V. Veerasubramanian, E. El-Fiky, D. Patel, and D. V. Plant, "A silicon photonic PAM-4 modulator based on dual-parallel Mach–Zehnder interferometers," *IEEE Photon. J.*, vol. 8, no. 1, Feb. 2016, Art. no. 7800610.
[30] A. Samani *et al.*, "Experimental parametric study of 128 Gb/s PAM-4 transmission system using a multi-electrode silicon photonic Mach Zehnder modulator," *Opt. Express*, vol. 25, no. 12, pp. 13252–13262, 2017.
[31] D. Patel, A. Samani, V. Veerasubramanian, S. Ghosh, and D. V. Plant, "Silicon photonic segmented modulator-based electro-optic DAC for 100 Gb/s PAM-4 generation," *IEEE Photon. Technol. Lett.*, vol. 27, no. 23, pp. 2433–2436, Dec. 2015.
[32] R. Dubé-Demers, S. LaRochelle, and W. Shi, "Low-power DAC-less PAM-4 transmitter using a cascaded microring modulator," *Opt. Lett.*, vol. 41, no. 22, pp. 5369–5372, 2016.
[33] R. Li *et al.*, "Analysis and experimental study of a silicon photonic single MRM-assisted MZI PAM-4 modulator," *IEEE Photon. J.*, vol. 9, no. 6, Dec. 2017, Art. no. 4900707.
[34] R. Li *et al.*, "Silicon photonic ring-assisted MZI for 50 Gb/s DAC-less and DSP-free PAM-4 transmission," *IEEE Photon. Technol. Lett.*, vol. 29, no. 12, pp. 1046–1049, Jun. 2017.
[35] *IEEE Standard for Ethernet - Amendment 10: Media Access Control Parameters, Physical Layers, and Management Parameters for 200 Gb/s and 400 Gb/s Operation*, IEEE Std 802.3bs-2017 (Amendment to IEEE 802.3-2015 as amended by IEEE's 802.3bw-2015, 802.3by-2016, 802.3bq-2016, 802.3bp-2016, 802.3br-2016, 802.3bn-2016, 802.3bz-2016, 802.3bu-2016, 802.3bv-2017, and IEEE 802.3-2015/Cor1-2017), 2017.
[36] J. Wang *et al.*, "Silicon high-speed binary phase-shift keying modulator with a single-drive push-pull high-speed traveling wave electrode," *Photon. Res.*, vol. 3, no. 3, pp. 58–62, 2015.
[37] M. Streshinsky *et al.*, "Low power 50 Gb/s silicon traveling wave Mach–Zehnder modulator near 1300 nm," *Opt. Express*, vol. 21, no. 25, pp. 30350–30357, 2013.
[38] M. Chagnon *et al.*, "Experimental study of 112 Gb/s short reach transmission employing PAM formats and SiP intensity modulator at 1.3 μm," *Opt. Express*, vol. 22, no. 17, pp. 21018–21036, 2014.
[39] C. Wang *et al.*, "Integrated lithium niobate electro-optic modulators operating at CMOS-compatible voltages," *Nature*, vol. 562, no. 7725, pp. 101–104, 2018.
[40] M. He *et al.*, "High-performance hybrid silicon and lithium niobate Mach–Zehnder modulators for 100 Gbit s^{-1} and beyond," *Nature Photon.*, vol. 13, no. 5, pp. 359–364, 2019.
[41] N. Qi *et al.*, "A 32 Gb/s NRZ, 25 GBaud/s PAM4 reconfigurable, Si-photonic MZM transmitter in CMOS," in *Proc. Opt. Fiber Commun. Conf. Exhib.*, 2016, Paper Th1F.3.
[42] C. Xiong *et al.*, "Monolithic 56 Gb/s silicon photonic pulse-amplitude modulation transmitter," *Optica*, vol. 3, no. 10, pp. 1060–1065, 2016.